Admittance Modeling and Stability Analysis of Grid-Connected Inverter with LADRC-PLL

Xie, Zhiwei; Chen, Yandong; Wu, Wenhua; Gong, Wenlan; Zhou, Leming; Zhou, Xiaoping; Guerrero, Josep M.

Published in:
IEEE Transactions on Industrial Electronics

DOI (link to publication from Publisher):
10.1109/TIE.2020.3044789

Publication date:
2021

Document Version
Accepted author manuscript, peer reviewed version

Admittance Modeling and Stability Analysis of Grid-Connected Inverter with LADRC-PLL

Zhiwei Xie, Yandong Chen, *Senior Member, IEEE*, Wenhua Wu, *Member, IEEE*, Wenlan Gong, Leming Zhou, *Member, IEEE*, Xiaoping Zhou, *Member, IEEE* and Josep M. Guerrero, *Fellow*, *IEEE*

***Abstract*—It tends to cause system oscillation when the inverter with a phase-locked loop based on proportional integral controller (PI-PLL) is connected to the weak grid. To improve the oscillation suppression ability of the grid-connected inverter, a linear active disturbance rejection controller is applied to PLL (LADRC-PLL). Considering the influence of linear extended state observer, voltage outer-loop, current inner-loop and frequency coupling, the admittance model of the grid-connected inverter with LADRC-PLL is established. Based on the established admittance model and the generalized Nyquist criterion, the system stabilities of the grid-connected inverters with LADRC-PLL and PI-PLL are compared. The comparison results indicate that the grid-connected inverter with LADRC-PLL has better adaptability to the weak grid and shows a certain ability to suppress the sub- and super-synchronous oscillation. Then, the influence of the control parameters of LADRC-PLL on the system stability is studied. It is found that the system keeps stable when the control parameter of LADRC-PLL is changed in a relatively wide range, which indicates LADRC-PLL has good robustness. Furthermore, the dynamic performances of the grid-connected inverters with LADRC-PLL and PI-PLL are analyzed. It is revealed that the grid-connected inverter with LADRC-PLL has better dynamic performance. Finally, the correctness of the analysis is verified by experiments.**

***Index Terms*—Admittance modeling, LADRC, stability analysis, sub- and super-synchronous oscillation.**

I. INTRODUCTION

WITH the increasing penetration of renewable energy (such as wind and solar) in the grid, the system oscillation frequently occurs when the renewable energy generator connected to the grid through the inverter. The system oscillation will result in the disconnection of the renewable energy generator, and even lead to the cutting off of the thermal power generator due to the shaft torsional vibrations, which seriously restricts the absorption of the renewable energy and threatens the stable operation of the grid [1].

In recent years, many researchers have devoted themselves to the study of the system oscillation when the inverter is connected to the weak grid [2]-[3]. The common research ideas are shown as follows: the system model is established firstly; then, the system stability is analyzed and the method to improve the system stability is proposed based on the established model. In the aspect of the grid-connected inverter system modeling, it is general to establish the small-signal impedance (admittance) model of the grid-connected inverter in frequency domain. The d-q impedance modeling method in synchronous coordinate system was proposed in [4]. Considering the influence of power outer-loop, current inner-loop and phase-locked loop (PLL), the d-q impedance model of the grid-connected inverter was established. Furthermore, it was proposed in [5] to establish the sequence impedance model for the grid-connected inverter in static coordinate system. The sequence impedance model has a clear physical meaning, can be widely applicated and is convenient to be verified by impedance measurement [6]-[7]. To analyze the mechanism of the system oscillation more accurately, an admittance model was established in [8] considering the influence of frequency coupling and voltage outer-loop.

In terms of stability analysis of the grid-connected inverter system, based on the established model, Nyquist criterion, generalized Nyqusit criterion or system poles can be used to explore the root cause of the system oscillation [9]-[11]. At present, it is generally believed that the mechanism of the system oscillation is the weak damping or negative damping oscillation produced by the interaction between the grid-connected inverter and the grid. The impedance-based method is adopted to analyze the influence of the short-circuit ratio (SCR), number and output power of wind turbines, and control parameters on the system oscillation [12]. The research shows that the grid-connected inverter of the permanent magnetic synchronous generator at its oscillation frequency presents the characteristic of "capacitive impedance with negative resistance" due to its control method, and forms weak damping or negative damping LC oscillation circuit with the inductive grid, which leads to the system oscillation. A lot of studies have shown that the PLL based on proportional integral controller (PI-PLL) is an important factor causing the sub- and super-synchronous oscillation in the grid-connected inverter system [13]-[22]. It is pointed out that PLL can affect the system oscillation mode of wind farms through the eigenvalue analysis method [13]. With the increasing of the PLL bandwidth, the system oscillation frequency increases, the stability margin decreases. The study in [14] shows that PLL affects the stability of current closed-loop control through the grid impedance, and the weaker the grid, the more obvious the coupling effect of PLL.

In order to suppress the adverse effects of PLL, there are many oscillation suppression methods, such as special device for oscillation suppression, control parameter optimization method, improved control strategy [15]-[16]. The static synchronous compensator (STATCOM) is applied to suppresses the sub-synchronous oscillation (SSR) in [17]. This method is convenient which uses the devices inside the renewable energy station to realize the oscillation suppression. However, STATCOM also have the risk of causing system stability problems due to their

Manuscript received August 26, 2020; revised October 31, 2020; accepted November 26, 2020. This work was supported in part by the National Key Research and Development Program of China (2017YFB0902000), in part by the China Postdoctoral Science Foundation under Grant (2020M682551) and in part by the Natural Science Foundation of Hunan Province (2020JJ5081).

Z. Xie, W. Wu, L. Zhou, and X. Zhou are with the College of Electrical and Information Engineering, Hunan University, Changsha 410082, China.

Y. Chen is with the College of Electrical and Information Engineering, Hunan University, Changsha 410082, China (Corresponding author, e-mail: yandong_chen@hnu.edu.cn).

W. Gong is with Electric Power Research Institute of Guangxi Power Grid Co. Ltd., Nanning 530023, China.

J. M. Guerrero is with the Department of Energy Technology, Aalborg University, Denmark.

interactions with AC power grid. It is proposed in [18] that reducing PLL bandwidth can strengthen system stability. What's more, an optimization design of the control parameter considering the influence of PLL and the grid impedance is put forward in [19] and the system stability is improved. Due to the consideration of the system dynamic performance, the optimization design of the control parameter cannot significantly enhance the system stability. In recent years, many researchers focus on the improved control strategy. The method reconstructing the impedance of the grid-connected inverter at the specified frequency area to enhance the system damping is suggested in [20], which effectively suppressed the sub- and super-synchronous oscillation. In [21], a voltage feed-forward oscillation suppression method is proposed. The adverse effects of PLL and the grid impedance on system stability can be offset by voltage feedforward control. It is mentioned in [22] that a virtual synchronous generator control strategy without PLL can be adopted to suppress the adverse effects of PLL and strengthen the system stability. The effectiveness of the improved control strategy makes it becomes the commonly method used to suppress the oscillation.

In 1999, J. Han systematically proposed active disturbance rejection control based on the study of classical regulation theory and modern control theory [23]. Then, Z. Gao linearized the controller and the extended state observer, and proposed linear active disturbance rejection controller (LADRC), which simplified the parameter tuning method of ADRC [24]. Since LADRC has the advantages of good tracking performance, anti-interference ability and the convenient for application, it is widely used in power electronic equipment such as DC converter, PWM rectifier and grid-connected inverter [25]-[28]. The control strategy of the grid-connected inverter plays an important role in the admittance characteristics and stability. However, the admittance characteristics of the grid-connected inverter with the PLL based on LADRC (LADRC-PLL) is rarely studied. What's more, there is no comprehensively comparative analysis about the admittance characteristics and the stability of the grid-connected inverters with LADRC-PLL and PI-PLL.

In this paper, admittance model of the grid-connected inverter with LADRC-PLL is established and its system stability is analyzed. The rest of this paper is organized as follows. The grid-connected inverter with LADRC-PLL is introduced in Section II. In Section III, considering the influence of linear extended state observer (LESO), voltage outer-loop, current inner-loop and frequency coupling, the admittance model of the grid-connected inverter with LADRC-PLL is established through harmonic linearization method. The admittance characteristics of the grid-connected inverters with LADRC-PLL and PI-PLL is verified and analyzed in Section IV. In Section V, based on the established admittance model and the generalized Nyquist criterion, the influence of SCR on the stability of the grid-connected inverters with LADRC-PLL and PI-PLL is analyzed; the robustness of control parameters on LADRC-PLL is studied; the dynamic performances of the grid-connected inverters with LADRC-PLL and PI-PLL are compared. Finally, the correctness of the analysis is verified by experiments in Section VI and some conclusions are drawn in Section VII.

II. The Grid-Connected Inverter With LADRC-PLL

A. Topology and control

The topology and control of the grid-connected inverter with LADRC-PLL are shown in Fig. 1, v_a, v_b and v_c are voltages in the point of common coupling (PCC). i_a, i_b and i_c are filter inductor currents of the grid-connected inverter. L_f, C_f and R_f are filter inductor, filter capacitor and damping resistor, respectively; L_g and R_g are equivalent line inductor and resistor of the grid, respectively. In Fig. 1, since the filter capacitor branch is not included in the control system, it can be regarded as a part of admittance of the grid-connected inverter as well as a part of the grid impedance. In this paper, Z_g shown in Fig. 1 is defined as the grid impedance and Y_{inv} presents the admittance of the grid-connected inverter.

The difference between the grid-connected inverter with LADRC-PLL and PI-PLL is the control strategy in PLL: one adopts LADRC, the other adopts PI controller. What's more, PI controllers are applied to voltage outer-loop and current inner-loop control of the grid-connected inverters:

$$G_v(s)=k_{p\_v}+\frac{k_{i\_v}}{s};\quad G_c(s)=k_{p\_c}+\frac{k_{i\_c}}{s} \tag{1}$$

where k_{p_v} and k_{p_c} are the proportional coefficients; k_{i_v} and k_{i_c} are the integral coefficients.

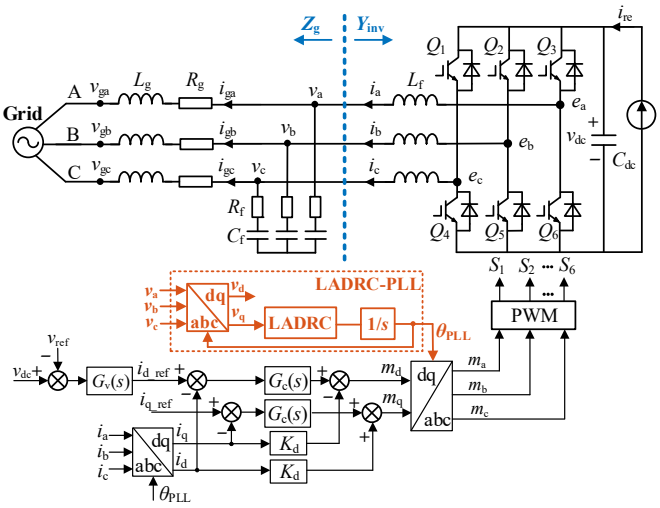

Fig. 1. The grid-connected inverter with LADRC-PLL.

B. The design of LADRC-PLL

The design process of LADRC-PLL starts with the PI-PLL which is shown in Fig. 2.

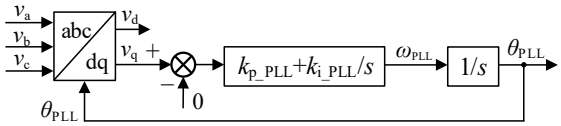

Fig. 2. The control block of PI-PLL.

When there is a small-disturbance in the system, the relationship between the actual phase of the voltage in PCC θ and the tracked phase of the PLL θ_{PLL} is shown in Fig. 3. Generally, the change of θ_{PLL} lags slightly behind that of θ. V_m is the amplitude of the voltage in PCC.

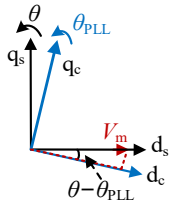

Fig. 3. The relationship between θ and θ_{PLL}.

According to Fig. 3, v_d and v_q can be expressed as follows.

$$\begin{bmatrix} v_d \\ v_q \end{bmatrix} = V_m \begin{bmatrix} \cos(\theta - \theta_{PLL}) \\ \sin(\theta - \theta_{PLL}) \end{bmatrix} \approx V_m \begin{bmatrix} 1 \\ \theta - \theta_{PLL} \end{bmatrix} \quad (2)$$

Therefore, the equivalent control structure of the linearized PI-PLL can be obtained from (2) and Fig. 2, as shown in Fig. 4.

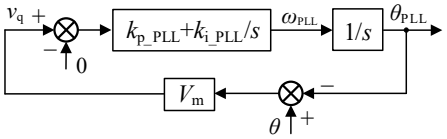

Fig. 4. The equivalent control structure of the linearized PI-PLL.

LADRC can be used to replace the PI control strategy in Fig. 4 to obtain LADRC-PLL. $y = v_q$ and $u = \omega_{PLL}$ are defined as the output signal and the input signal of the control object of LADRC, respectively. Thus, the differential equation of the control object of LADRC is shown as (3).

$$\begin{aligned} & y = V_m(-\frac{u}{s} + \theta) \\ \Rightarrow\ & \dot{y} = -V_m u + \dot{\theta} \\ \Rightarrow\ & \dot{y} = b_0 u + f_d \end{aligned} \quad (3)$$

where the input gain $b_0 = -V_m$, the disturbance $f_d = \dot{\theta}$.

According to (3), the controlled object is a first-order system. Therefore, the typical first-order LADRC can be adopted. The designed control structure of LADRC-PLL is shown in Fig. 5. LADRC is mainly composed of LESO, linear error feedback control law and disturbance compensation.

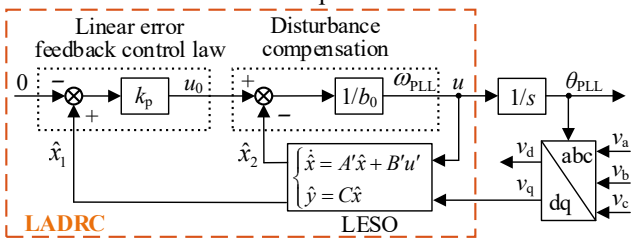

Fig. 5. The designed control structure of LADRC-PLL.

C. The design of the parameters in LADRC-PLL

LESO is used to estimate v_q and f_d. It is defined that $x_1 = y$, $x_2 = f_d$, $h = \dot{f}_d$, (3) can be transformed to the form of state space model as follows.

$$\begin{cases} \dot{x} = Ax + Bu + Eh \\ y = Cx \end{cases} \quad (4)$$

where $A = [0, 1; 0, 0]$, $B = [b_0, 0]^T$, $C = [1, 0]$, $E = [0, 1]^T$.

The Luenberger observer is adopted to construct LESO, as shown in (5).

$$\begin{cases} \dot{\hat{x}} = A\hat{x} + Bu + L(y - \hat{y}) = \underbrace{(A - LC)}_{A'}\hat{x} + \underbrace{(B \quad L)}_{B'}\underbrace{(u \quad y)^T}_{u'} \\ \hat{y} = C\hat{x} \end{cases} \quad (5)$$

where $\hat{x}_1$, $\hat{x}_2$ and $\hat{y}$ are the estimated value of x_1, x_2 and y. The system matrix $A' = [-\beta_1, 1; -\beta_2, 0]$, the observer gains matrix $L = [\beta_1, \beta_2]^T$, the input matrix $B' = [b_0, \beta_1; 0, \beta_2]$.

Therefore, the LESO can be modeled as below.

$$\begin{bmatrix} \dot{\hat{x}}_1 \\ \dot{\hat{x}}_2 \end{bmatrix} = \begin{bmatrix} -\beta_1 & 1 \\ -\beta_2 & 0 \end{bmatrix}\begin{bmatrix} \hat{x}_1 \\ \hat{x}_2 \end{bmatrix} + \begin{bmatrix} b_0 & \beta_1 \\ 0 & \beta_2 \end{bmatrix}\begin{bmatrix} u \\ y \end{bmatrix} \quad (6)$$

According to (6), the LESO can be realized in the digital controller to make the v_q and f_d can be estimated in real time.

The characteristic polynomial of LESO is shown as follows.

$$\lambda(s) = |sI - A'| = s^2 + \beta_1 s + \beta_2 \quad (7)$$

With reference to the bandwidth tuning method proposed by Z. Gao [24], the characteristic roots are obtained as $\beta_1 = 2\omega_0$, $\beta_2 = \omega_0^2$, ω_0 is the observer bandwidth.

Due to $\hat{x}_2 \approx x_2 = f_d$ (it is valid within the designed ω_0), the differential equation of LADRC-PLL is expressed as follows:

$$\dot{y} = f_d + u_0 - \hat{x}_2 = u_0 + (f_d - \hat{x}_2) \approx u_0 \quad (8)$$

where u_o is obtained from linear error feedback control law:

$$u_0 = k_p(\hat{x}_1 - r),$$

r is the set value of the controller, $r = 0$ in PLL.

The expected closed-loop transfer function of the system can be obtained by (8) after the Laplace transformation.

$$\frac{Y(s)}{R(s)} = \frac{-k_p}{s - k_p} \quad (9)$$

where $Y(s)$ and $R(s)$ are the expressions of y and r after the Laplace transformation; the controller bandwidth $\omega_c = -k_p$.

III. Admittance Modeling of the Grid-Connected Inverter With LADRC-PLL

Considering the influence of LESO, voltage outer-loop, current inner-loop and frequency coupling, the admittance model of the grid-connected inverter with LADRC-PLL is derived by harmonic linearization method.

When a positive-sequence voltage perturbation at the perturbation frequency f_p is injected into the grid-connected inverter system, it will generate a positive-sequence response current at f_p and a negative-sequence response current at the coupling frequency $f_{p1} = f_p - 2f_1$. Due to the existence of the grid impedance, a negative-sequence voltage at f_{p1} will occur in PCC. Thus, after the voltage perturbation is injected, the expressions of v_a and i_a in time-domain are shown as follows.

$$\begin{aligned} v_a(t) = & V_1\cos(2\pi f_1 t) + V_p\cos(2\pi f_p t + \varphi_{vp}) \\ & + V_{p1}\cos(2\pi f_{p1} t + \varphi_{vp1}) \end{aligned} \quad (10)$$

$$\begin{aligned} i_a(t) = & I_1\cos(2\pi f_1 t + \varphi_{i1}) + I_p\cos(2\pi f_p t + \varphi_{ip}) \\ & + I_{p1}\cos(2\pi f_{p1} t + \varphi_{ip1}) \end{aligned} \quad (11)$$

where f_1 is the fundamental frequency; V_1, V_p, V_{p1}, I_1, I_p and I_{p1} are the amplitudes of the corresponding voltage and current, respectively; φ_{vp}, φ_{vp1}, φ_{i1}, φ_{ip} and φ_{ip1} are the initial phase of the corresponding voltage and current, respectively. The expressions of v_a and i_a in frequency-domain can be obtained as below.

$$\mathbf{V}_a[f] = \begin{cases} \mathbf{V}_1, & f = \pm f_1 \\ \mathbf{V}_p, & f = \pm f_p \\ \mathbf{V}_{p1}, & f = \pm f_{p1} \end{cases}, \quad \mathbf{I}_a[f] = \begin{cases} \mathbf{I}_1, & f = \pm f_1 \\ \mathbf{I}_p, & f = \pm f_p \\ \mathbf{I}_{p1}, & f = \pm f_{p1} \end{cases} \quad (12)$$

where $\mathbf{V}_1 = V_1/2$, $\mathbf{V}_p = (V_p/2)e^{\pm j\varphi_{vp}}$, $\mathbf{V}_{p1} = (V_{p1}/2)e^{\pm j\varphi_{vp1}}$, $\mathbf{I}_1 = (I_1/2)e^{\pm j\varphi_{i1}}$, $\mathbf{I}_p = (I_p/2)e^{\pm j\varphi_{ip}}$, $\mathbf{I}_{p1} = (I_{p1}/2)e^{\pm j\varphi_{ip1}}$.

The Park's transformation and the inverse Park's transformation in Fig. 1 are defined as (13) and (14), respectively.

$$T(\theta_{PLL}) = \frac{2}{3}\begin{bmatrix} \cos\theta_{PLL} & \cos(\theta_{PLL} - 2\pi/3) & \cos(\theta_{PLL} + 2\pi/3) \\ -\sin\theta_{PLL} & -\sin(\theta_{PLL} - 2\pi/3) & -\sin(\theta_{PLL} + 2\pi/3) \\ 1/2 & 1/2 & 1/2 \end{bmatrix} \quad (13)$$

$$\mathrm{T}^{-1}\left(\theta_{\mathrm{PLL}}\right)=\begin{bmatrix}\cos\theta_{\mathrm{PLL}} & -\sin\theta_{\mathrm{PLL}} & 1\\ \cos\left(\theta_{\mathrm{PLL}}-2\pi/3\right) & -\sin\left(\theta_{\mathrm{PLL}}-2\pi/3\right) & 1\\ \cos\left(\theta_{\mathrm{PLL}}+2\pi/3\right) & -\sin\left(\theta_{\mathrm{PLL}}+2\pi/3\right) & 1\end{bmatrix} \quad (14)$$

A. LADRC-PLL modeling

According to (6), the transfer function model of LESO can be represented as Fig. 6. $\hat{x}_1$ and $\hat{x}_2$ are both affected by y and u. The expressions of $\hat{x}_1$ and $\hat{x}_2$ are obtained with the superposition principle, as shown in (15) and (16).

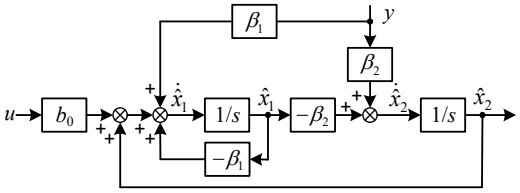

Fig. 6. The transfer function model of LESO.

$$\hat{x}_1=\frac{2\omega_0 s+\omega_0^2}{\left(s+\omega_0\right)^2}v_{\mathrm{q}}+\frac{b_0 s}{\left(s+\omega_0\right)^2}\omega_{\mathrm{PLL}} \quad (15)$$

$$\hat{x}_2=\frac{\omega_0^2 s}{\left(s+\omega_0\right)^2}v_{\mathrm{q}}-\frac{b_0\omega_0^2}{\left(s+\omega_0\right)^2}\omega_{\mathrm{PLL}} \quad (16)$$

According to the designed control structure of LADRC-PLL shown in Fig. 5, the following relationship can be obtained:

$$\left(\hat{x}_1 k_{\mathrm{p}}-\hat{x}_2\right)\frac{1}{b_0}\cdot\frac{1}{s}=\theta_{\mathrm{PLL}} \quad (17)$$

where $\theta_{\mathrm{PLL}}=\omega_{\mathrm{PLL}}/s$. Submitting (15) and (16) to (17), (18) can be derived.

$$\theta_{\mathrm{PLL}}=\frac{\left(2k_{\mathrm{p}}-\omega_0\right)\omega_0 s+k_{\mathrm{p}}\omega_0^2}{b_0 s^3+\left(2\omega_0-k_{\mathrm{p}}\right)b_0 s^2}v_{\mathrm{q}} \quad (18)$$

The transfer function between θ_{PLL} and v_{q} can be defined as:

$$G_{\mathrm{PLL}}\left(s\right)=\frac{\left(2k_{\mathrm{p}}-\omega_0\right)\omega_0 s+k_{\mathrm{p}}\omega_0^2}{b_0 s^3+\left(2\omega_0-k_{\mathrm{p}}\right)b_0 s^2} \quad (19)$$

Considering that LADRC-PLL is affected by disturbance, the output of LADRC-PLL is expressed as $\theta_{\mathrm{PLL}}(t)=\Delta\theta_{\mathrm{PLL}}(t)+\theta_1(t)$. Therefore, (13) and (14) can be derived as:

$$\mathrm{T}\left(\theta_{\mathrm{PLL}}\left(t\right)\right)=\begin{bmatrix}\cos\left(\Delta\theta_{\mathrm{PLL}}\left(t\right)\right) & \sin\left(\Delta\theta_{\mathrm{PLL}}\left(t\right)\right) & 0\\ -\sin\left(\Delta\theta_{\mathrm{PLL}}\left(t\right)\right) & \cos\left(\Delta\theta_{\mathrm{PLL}}\left(t\right)\right) & 0\\ 0 & 0 & 1\end{bmatrix}\mathrm{T}\left(\theta_1\left(t\right)\right) \quad (20)$$

$$\mathrm{T}^{-1}\left(\theta_{\mathrm{PLL}}\left(t\right)\right)=\mathrm{T}^{-1}\left(\theta_1\left(t\right)\right)\begin{bmatrix}\cos\left(\Delta\theta_{\mathrm{PLL}}\left(t\right)\right) & -\sin\left(\Delta\theta_{\mathrm{PLL}}\left(t\right)\right) & 0\\ \sin\left(\Delta\theta_{\mathrm{PLL}}\left(t\right)\right) & \cos\left(\Delta\theta_{\mathrm{PLL}}\left(t\right)\right) & 0\\ 0 & 0 & 1\end{bmatrix} \quad (21)$$

The expressions of v_{d}, v_{q}, i_{d} and i_{q} in frequency domain can be obtained from the Park's transformation in (20).

According to the derivation in [5], the relationship between $\Delta\theta_{\mathrm{PLL}}$ and $\mathbf{V}_{\mathrm{p}}$, $\mathbf{V}_{\mathrm{p1}}$ at $f=\pm(f_{\mathrm{p}}-f_1)$ can be obtained as follows:

$$\begin{cases}\Delta\theta_{\mathrm{PLL}}[f]=T_{\mathrm{p}}\left(s_2\right)\mathbf{V}_{\mathrm{p}}+T_{\mathrm{p1}}\left(s_2\right)\mathbf{V}_{\mathrm{p1}}\\ T_{\mathrm{p}}\left(s\right)=\dfrac{\mp jG_{\mathrm{PLL}}\left(s\right)}{1+V_1 G_{\mathrm{PLL}}\left(s\right)},T_{\mathrm{p1}}\left(s\right)=\dfrac{\pm jG_{\mathrm{PLL}}\left(s\right)}{1+V_1 G_{\mathrm{PLL}}\left(s\right)}\end{cases} \quad (22)$$

B. Voltage outer-loop modeling

When the switch loss of the grid-connected inverter is ignored, the power on the DC-side is equal to the power on the AC-side. Therefore, (23) can be obtained.

$$\begin{aligned}\left(i_{\mathrm{re}}-sC_{\mathrm{dc}}v_{\mathrm{dc}}\right)v_{\mathrm{dc}}=&\left(v_{\mathrm{a}}+sL_{\mathrm{f}}i_{\mathrm{a}}\right)i_{\mathrm{a}}+\left(v_{\mathrm{b}}+sL_{\mathrm{f}}i_{\mathrm{b}}\right)i_{\mathrm{b}}\\&+\left(v_{\mathrm{c}}+sL_{\mathrm{f}}i_{\mathrm{c}}\right)i_{\mathrm{c}}\end{aligned} \quad (23)$$

The expression of DC-side voltage at frequency $f=\pm(f_{\mathrm{p}}-f_1)$ can be derived through (23).

$$v_{\mathrm{dc}}[f]=\frac{3\left[\left(\mathbf{V}_1^*+s_2L_{\mathrm{f}}\mathbf{I}_1^*\right)\mathbf{I}_{\mathrm{p}}+\left(s_2L_{\mathrm{f}}\mathbf{I}_1+\mathbf{V}_1\right)\mathbf{I}_{\mathrm{p1}}+\mathbf{I}_1^*\mathbf{V}_{\mathrm{p}}\mathbf{I}_1+\mathbf{V}_{\mathrm{p1}}\right]}{i_{\mathrm{re}}-s_2C_{\mathrm{dc}}V_{\mathrm{dc}}} \quad (24)$$

where $s_2=\pm(j2\pi f_{\mathrm{p}}-j2\pi f_1)$, V_{dc} is the steady-state component of $v_{\mathrm{dc}}[f]$. What's more, $v_{\mathrm{dc}}[f]$ can be expressed as:

$$v_{\mathrm{dc}}\left[f\right]=A_{\mathrm{i1}}\mathbf{I}_{\mathrm{p}}+A_{\mathrm{i2}}\mathbf{I}_{\mathrm{p1}}+A_{\mathrm{v1}}\mathbf{V}_{\mathrm{p}}+A_{\mathrm{v2}}\mathbf{V}_{\mathrm{p1}} \quad (25)$$

where

$$\begin{bmatrix}A_{\mathrm{i1}} & A_{\mathrm{i2}}\\ A_{\mathrm{v1}} & A_{\mathrm{v2}}\end{bmatrix}=\begin{bmatrix}\dfrac{3\left(\mathbf{V}_1^*+s_2L_{\mathrm{f}}\mathbf{I}_1^*\right)}{i_{\mathrm{re}}-s_2C_{\mathrm{dc}}V_{\mathrm{dc}}} & \dfrac{3\left(\mathbf{V}_1+s_2L_{\mathrm{f}}\mathbf{I}_1\right)}{i_{\mathrm{re}}-s_2C_{\mathrm{dc}}V_{\mathrm{dc}}}\\ \dfrac{3\mathbf{I}_1^*}{i_{\mathrm{re}}-s_2C_{\mathrm{dc}}V_{\mathrm{dc}}} & \dfrac{3\mathbf{I}_1}{i_{\mathrm{re}}-s_2C_{\mathrm{dc}}V_{\mathrm{dc}}}\end{bmatrix}.$$

In order to simplify the expression, it can be defined that $s=\pm j2\pi f_{\mathrm{p}}$, $s_1=\pm j2\pi f_1$, $s_{\mathrm{p1}}=\pm(j2\pi f_{\mathrm{p}}-j4\pi f_1)$.

C. Current inner-loop modeling

According to the control method of the grid-connected inverter with LADRC-PLL shown in Fig. 1, the expressions of the modulation signal m_{d} and m_{q} can be obtained.

$$\begin{bmatrix}m_{\mathrm{d}}\\ m_{\mathrm{q}}\end{bmatrix}=\begin{bmatrix}\left[\left(v_{\mathrm{dc}}-v_{\mathrm{ref}}\right)G_{\mathrm{v}}\left(s\right)-i_{\mathrm{d}}\right]G_{\mathrm{i}}\left(s\right)-K_{\mathrm{d}}i_{\mathrm{q}}\\ \left(i_{\mathrm{q\_ref}}-i_{\mathrm{q}}\right)G_{\mathrm{i}}\left(s\right)+K_{\mathrm{d}}i_{\mathrm{d}}\end{bmatrix} \quad (26)$$

where v_{ref} is the reference value of the DC-side voltage, $i_{\mathrm{q\_ref}}$ is the reference value of the filter inductor current in q-axis.

The fundamental component m_1 in m_{a} is shown in (27).

$$m_1=\frac{\mathbf{V}_1+s_1L_{\mathrm{f}}\mathbf{I}_1}{K_{\mathrm{pwm}}v_{\mathrm{ref}}} \quad (27)$$

The expressions of m_{d} and m_{q} are obtained from (26) and (27).

$$m_{\mathrm{d}}=\begin{cases}m_{\mathrm{d0}} & ,\mathrm{dc}\\ \left(v_{\mathrm{dc}}\left(s_2\right)G_{\mathrm{v}}\left(s_2\right)-i_{\mathrm{d}}\left(s_2\right)\right)G_{\mathrm{i}}\left(s_2\right)- & \\ K_{\mathrm{d}}i_{\mathrm{q}}\left(s_2\right) & ,f=\pm\left(f_{\mathrm{p}}-f_1\right)\end{cases} \quad (28)$$

$$m_{\mathrm{q}}=\begin{cases}m_{\mathrm{q0}} & ,\mathrm{dc}\\ -i_{\mathrm{q}}\left(s_2\right)G_{\mathrm{i}}\left(s_2\right)+K_{\mathrm{d}}i_{\mathrm{d}}\left(s_2\right), & f=\pm\left(f_{\mathrm{p}}-f_1\right)\end{cases} \quad (29)$$

where m_{d0} and m_{q0} are the real part and imaginary part of m_1, respectively.

After m_{d} and m_{q} are transformed into static coordinate system by the inverse Park's transformation in (21), m_{a} can be obtained.

$$\begin{aligned}m_{\mathrm{a}}=&\cos\left(\theta_1[f]\right)\otimes\left(m_{\mathrm{d}}[f]-\Delta\theta_{\mathrm{PLL}}[f]\otimes m_{\mathrm{q}}[f]\right)-\\&\sin\left(\theta_1[f]\right)\otimes\left(\Delta\theta_{\mathrm{PLL}}[f]\otimes m_{\mathrm{d}}[f]+m_{\mathrm{q}}[f]\right)\end{aligned} \quad (30)$$

where the symbol "⊗" denotes convolution calculation.

D. Admittance modeling

The system in Fig. 1 has the following relationship.

$$sL_{\mathrm{f}}i_{\mathrm{a}} = K_{\mathrm{pwm}}v_{\mathrm{dc}}m_{\mathrm{a}} - v_{\mathrm{a}} \tag{31}$$

where K_{pwm} is the modulation coefficient.

According to (12), (30) and (31), the relationship between the disturbance voltage in v_{a} and the response current in i_{a} is obtained.

$$-\begin{bmatrix}\mathbf{I}_{\mathrm{p}}\\ \mathbf{I}_{\mathrm{p1}}\end{bmatrix} = \begin{bmatrix}Y_{11\mathrm{L}} & Y_{12\mathrm{L}}\\ Y_{21\mathrm{L}} & Y_{22\mathrm{L}}\end{bmatrix}\begin{bmatrix}\mathbf{V}_{\mathrm{p}}\\ \mathbf{V}_{\mathrm{p1}}\end{bmatrix} \tag{32}$$

$$Y_{11\mathrm{L}} = \frac{-\left[s_{\mathrm{p1}}L_{\mathrm{f}} - \left(0.5A_{\mathrm{i2}}D_{\mathrm{v2}} + G_{\mathrm{i2}}\right)K_{\mathrm{pwm}}\right]\left[\left(0.5A_{\mathrm{v1}}D_{\mathrm{v1}} + H_{\mathrm{v1}} + B_{\mathrm{v1}}\right)K_{\mathrm{pwm}} - 1\right] - 0.5A_{\mathrm{i2}}D_{\mathrm{v1}}\left(0.5A_{\mathrm{v1}}D_{\mathrm{v2}} + H_{\mathrm{v3}} + B_{\mathrm{v3}}\right)K_{\mathrm{pwm}}^2}{\left[sL_{\mathrm{f}} - \left(0.5A_{\mathrm{i1}}D_{\mathrm{v1}} + G_{\mathrm{i1}}\right)K_{\mathrm{pwm}}\right]\left[s_{\mathrm{p1}}L_{\mathrm{f}} - \left(0.5A_{\mathrm{i2}}D_{\mathrm{v2}} + G_{\mathrm{i2}}\right)K_{\mathrm{pwm}}\right] - 0.25A_{\mathrm{i2}}D_{\mathrm{v1}}A_{\mathrm{i1}}D_{\mathrm{v2}}K_{\mathrm{pwm}}^2} \tag{33}$$

$$Y_{12\mathrm{L}} = \frac{\left\{-\left[s_{\mathrm{p1}}L_{\mathrm{f}} - \left(0.5A_{\mathrm{i2}}D_{\mathrm{v2}} + G_{\mathrm{i2}}\right)K_{\mathrm{pwm}}\right]\left(0.5A_{\mathrm{v2}}D_{\mathrm{v1}} + H_{\mathrm{v2}} + B_{\mathrm{v2}}\right) - 0.5A_{\mathrm{i2}}D_{\mathrm{v1}}\left[\left(0.5A_{\mathrm{v2}}D_{\mathrm{v2}} + H_{\mathrm{v4}} + B_{\mathrm{v4}}\right)K_{\mathrm{pwm}} - 1\right]\right\}K_{\mathrm{pwm}}}{\left[sL_{\mathrm{f}} - \left(0.5F_{\mathrm{i}}D_{\mathrm{v1}} + G_{\mathrm{i1}}\right)K_{\mathrm{pwm}}\right]\left[s_{\mathrm{p1}}L_{\mathrm{f}} - \left(0.5A_{\mathrm{i2}}D_{\mathrm{v2}} + G_{\mathrm{i2}}\right)K_{\mathrm{pwm}}\right] - 0.25A_{\mathrm{i2}}D_{\mathrm{v1}}A_{\mathrm{i1}}D_{\mathrm{v2}}K_{\mathrm{pwm}}^2} \tag{34}$$

$$Y_{21\mathrm{L}} = \frac{\left\{-0.5A_{\mathrm{i1}}D_{\mathrm{v2}}\left[\left(0.5A_{\mathrm{v1}}D_{\mathrm{v1}} + H_{\mathrm{v1}} + B_{\mathrm{v1}}\right)K_{\mathrm{pwm}} - 1\right] - \left[sL_{\mathrm{f}} - \left(0.5A_{\mathrm{i1}}D_{\mathrm{v1}} + G_{\mathrm{i1}}\right)K_{\mathrm{pwm}}\right]\left(0.5A_{\mathrm{v1}}D_{\mathrm{v2}} + H_{\mathrm{v3}} + B_{\mathrm{v3}}\right)\right\}K_{\mathrm{pwm}}}{\left[sL_{\mathrm{f}} - \left(0.5A_{\mathrm{i1}}D_{\mathrm{v1}} + G_{\mathrm{i1}}\right)K_{\mathrm{pwm}}\right]\left[s_{\mathrm{p1}}L_{\mathrm{f}} - \left(0.5A_{\mathrm{i2}}D_{\mathrm{v2}} + G_{\mathrm{i2}}\right)K_{\mathrm{pwm}}\right] - 0.25A_{\mathrm{i2}}D_{\mathrm{v1}}A_{\mathrm{i1}}D_{\mathrm{v2}}K_{\mathrm{pwm}}^2} \tag{35}$$

$$Y_{22\mathrm{L}} = \frac{-0.5A_{\mathrm{i1}}D_{\mathrm{v2}}\left(0.5A_{\mathrm{v2}}D_{\mathrm{v1}} + H_{\mathrm{v2}} + B_{\mathrm{v2}}\right)K_{\mathrm{pwm}}^2 - \left[sL_{\mathrm{f}} - \left(0.5A_{\mathrm{i1}}D_{\mathrm{v1}} + G_{\mathrm{i1}}\right)K_{\mathrm{pwm}}\right]\left[\left(0.5A_{\mathrm{v2}}D_{\mathrm{v2}} + H_{\mathrm{v4}} + B_{\mathrm{v4}}\right)K_{\mathrm{pwm}} - 1\right]}{\left[sL_{\mathrm{f}} - \left(0.5A_{\mathrm{i1}}D_{\mathrm{v1}} + G_{\mathrm{i1}}\right)K_{\mathrm{pwm}}\right]\left[s_{\mathrm{p1}}L_{\mathrm{f}} - \left(0.5A_{\mathrm{i2}}D_{\mathrm{v2}} + G_{\mathrm{i2}}\right)K_{\mathrm{pwm}}\right] - 0.25A_{\mathrm{i2}}D_{\mathrm{v1}}A_{\mathrm{i1}}D_{\mathrm{v2}}K_{\mathrm{pwm}}^2} \tag{36}$$

In (32), $Y_{11\mathrm{L}}$ and $Y_{22\mathrm{L}}$ are sequence admittances of the grid-connected inverter with LADRC-PLL, $Y_{12\mathrm{L}}$ and $Y_{21\mathrm{L}}$ are coupling admittances of the grid-connected inverter with LADRC-PLL, and their expressions are shown in (33)-(36). The expressions of the variables in (33)-(36) are shown as (37)-(40).

$$\begin{cases} B_{\mathrm{v1}} = \left[K_{\mathrm{d}}\mathbf{I}_{\mathrm{1}} + 0.5\left(\pm jm_{\mathrm{d0}} - m_{\mathrm{q0}}\right)\right]T_{\mathrm{p}}\left(s_2\right)V_{\mathrm{dc}} \\ B_{\mathrm{v2}} = \left[K_{\mathrm{d}}\mathbf{I}_{\mathrm{1}} + 0.5\left(\pm jm_{\mathrm{d0}} - m_{\mathrm{q0}}\right)\right]T_{\mathrm{p1}}\left(s_2\right)V_{\mathrm{dc}} \\ B_{\mathrm{v3}} = \left[K_{\mathrm{d}}\mathbf{I}_{\mathrm{1}}^{*} + 0.5\left(\mp jm_{\mathrm{d0}} - m_{\mathrm{q0}}\right)\right]T_{\mathrm{p}}\left(s_2\right)V_{\mathrm{dc}} \\ B_{\mathrm{v4}} = \left[K_{\mathrm{d}}\mathbf{I}_{\mathrm{1}}^{*} + 0.5\left(\mp jm_{\mathrm{d0}} - m_{\mathrm{q0}}\right)\right]T_{\mathrm{p1}}\left(s_2\right)V_{\mathrm{dc}} \end{cases} \tag{37}$$

$$\begin{bmatrix}D_{\mathrm{v1}}\\ D_{\mathrm{v2}}\end{bmatrix} = \begin{bmatrix}V_{\mathrm{dc}}G_{\mathrm{v}}\left(s_2\right)G_{\mathrm{c}}\left(s_2\right) + m_{\mathrm{1}}\\ V_{\mathrm{dc}}G_{\mathrm{v}}\left(s_2\right)G_{\mathrm{c}}\left(s_2\right) + m_{\mathrm{1}}^{*}\end{bmatrix} \tag{38}$$

$$\begin{cases} G_{\mathrm{i1}} = \left(-G_{\mathrm{c}}\left(s_2\right) \pm jK_{\mathrm{d}}\right)V_{\mathrm{dc}} \\ G_{\mathrm{i2}} = \left(-G_{\mathrm{c}}\left(s_2\right) \mp jK_{\mathrm{d}}\right)V_{\mathrm{dc}} \end{cases} \tag{39}$$

$$\begin{cases} H_{\mathrm{v1}} = \pm jG_{\mathrm{c}}\left(s_2\right)V_{\mathrm{dc}}\mathbf{I}_{\mathrm{1}}^{*}T_{\mathrm{p}}\left(s_2\right) \\ H_{\mathrm{v2}} = \pm jG_{\mathrm{c}}\left(s_2\right)V_{\mathrm{dc}}\mathbf{I}_{\mathrm{1}}T_{\mathrm{p1}}\left(s_2\right) \\ H_{\mathrm{v3}} = \mp jG_{\mathrm{c}}\left(s_2\right)V_{\mathrm{dc}}\mathbf{I}_{\mathrm{1}}^{*}T_{\mathrm{p}}\left(s_2\right) \\ H_{\mathrm{v4}} = \mp jG_{\mathrm{c}}\left(s_2\right)V_{\mathrm{dc}}\mathbf{I}_{\mathrm{1}}T_{\mathrm{p1}}\left(s_2\right) \end{cases} \tag{40}$$

IV. Verification and Characteristic Analysis of the Admittance Model

The parameters of the grid-connected inverter with LADRC-PLL are shown in Table I. ω_0 is generally larger than ω_{c} and usually chosen with the consideration of the speed of states estimation and noise sensitivity [29]. In this paper, ω_0 = $1.5\omega_{\mathrm{c}}$ and ω_{c} = 120 rad/s. To verify the correctness of the established admittance model, an admittance measurement simulation platform is built in Matlab/Simulink. The admittance measurement results of the grid-connected inverter with LADRC-PLL are shown in Fig. 7. The red solid line shows the established admittance model of the grid-connected inverter with LADRC-PLL, and the red circle represents the admittance measurement result. It can be seen from Fig. 7 that the admittance measurement results are in good agreement with the established admittance model, which proves the correctness of the built admittance model.

There are many control methods of PLL emerged in recent years [30]-[32]. In the communication with the manufacturers of grid-connected inverters, it is found that most PLLs of the grid-connected inverters still adopt PI control in synchronous coordinate system. PI-PLL is the typical PLL. Therefore, this paper will focus on the comparison between LADRC-PLL and PI-PLL.

TABLE I

PARAMETERS OF THE GRID-CONNECTED INVERTER WITH LADRC-PLL

Parameters	value	Parameters	value
L_{f} (mH)	0.15	$k_{\mathrm{p\_c}}$	3.08×10^{-4}
C_{f} (μF)	500	$k_{\mathrm{i\_c}}$	0.55
R_{f} (Ω)	0.02	$k_{\mathrm{p\_v}}$	5.21
C_{dc} (μF)	10000	$k_{\mathrm{i\_v}}$	719.99
i_{re} (A)	1153.85	K_{d}	7.25×10^{-5}
f_{s} (kHz)	4.50	K_{pwm}	0.5
V_{1} (V)	563.38	b_0	-563
f_{1} (Hz)	50	ω_{c} (rad/s)	120
$i_{\mathrm{q\_ref}}$ (A)	0	ω_0 (rad/s)	180
v_{ref} (V)	1300	k_{p}	-120

The admittance model of the grid-connected inverter with PI-PLL can be defined as (41).

$$-\begin{bmatrix}\mathbf{I}_{\mathrm{p}}\\ \mathbf{I}_{\mathrm{p1}}\end{bmatrix} = \begin{bmatrix}Y_{11\mathrm{P}} & Y_{12\mathrm{P}}\\ Y_{21\mathrm{P}} & Y_{22\mathrm{P}}\end{bmatrix}\begin{bmatrix}\mathbf{V}_{\mathrm{p}}\\ \mathbf{V}_{\mathrm{p1}}\end{bmatrix} \tag{41}$$

In PI-PLL, $k_{\mathrm{p\_PLL}}$ = 8.90×10^{-2}, $k_{\mathrm{i\_PLL}}$ = 33.28. The other parameters of the grid-connected inverter with PI-PLL are consistent with those of the grid-connected inverter with LADRC-PLL. The admittance characteristic curves and simulation measurement results of the grid-connected inverter with PI-PLL are shown in Fig. 7. The black solid line represents the admittance model of grid-connected inverter with PI-PLL, and the black plus indicates the admittance measurement result.

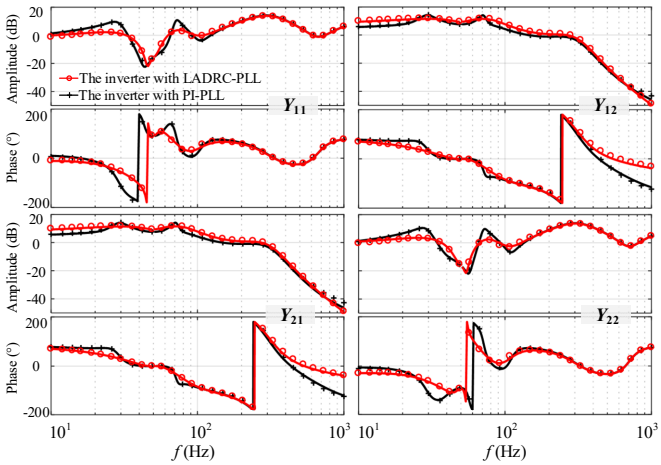

Fig. 7. Admittance characteristic curves.

The amplitude difference between the grid-connected inverters with LADCR-PLL and PI-PLL is shown in Fig. 8, the phase difference between the grid-connected inverters with LADCR-PLL and PI-PLL is shown in Fig. 9. The four pictures in Fig. 8 (Fig. 9) are used to present the amplitude differences (the phase differences) of the elements in the admittance matrix, respectively.

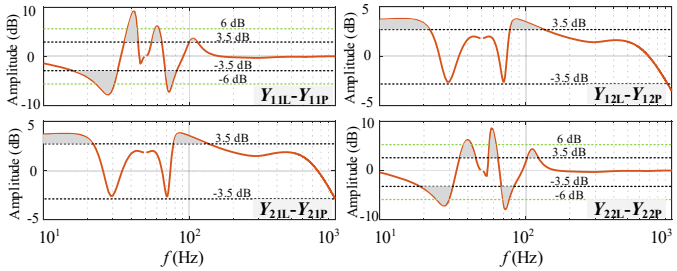

Fig. 8. The amplitude differences between the grid-connected inverters with LADCR-PLL and PI-PLL.

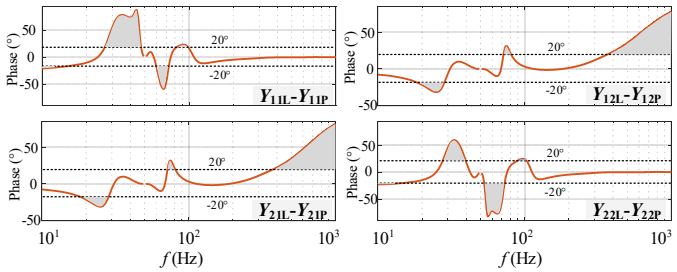

Fig. 9. The phase differences between the grid-connected inverters with LADCR-PLL and PI-PLL.

As shown in Fig. 8 and Fig. 9, the admittance characteristics of the grid-connected inverter is changed in wide bandwidth when PI-PLL is replaced with LADRC-PLL. 1) In the sub- and super-synchronous frequency area (20 Hz to 80 Hz), after replacing PI-PLL with LADRC-PLL, the positive resistive components of the admittances are increased and the system damping is enhanced which reduces the risk of oscillation and improves the system stability. 2) In the high frequency area (larger than 300 Hz), the coupling admittances of the grid-connected inverter are changed after adopting LADRC-PLL. However, the system stability of the grid-connected inverter with LADRC-PLL is dominated by the sequence admittances in the high frequency area. Due to the sequence admittances never changes, the system stability barely changes when the PI-PLL is replaced by LADRC-PLL in the high frequency area.

Based on the established admittance model, the stability of the grid-connected inverters with LADRC-PLL and PI-PLL will be analyzed, and their dynamic performances will be compared.

V. Analysis of Operation Characteristics of Grid-Connected Inverter Systems

A. Stability analysis when SCR is changed

The stability analysis of the grid-connected inverters with LADRC-PLL and PI-PLL are based on the generalized Nyquist criterion. λ_1 and λ_2 are defined as the two eigenvalues of the system return rate matrix shown in (42). The stability of the system is judged according to the Nyquist plots of λ_1 and λ_2 and the dotted line represents λ_1 and the solid line represents λ_2.

$$L=Z_g \cdot Y_{inv}=\begin{bmatrix} Z_{g11}\cdot Y_{11} & Z_{g11}\cdot Y_{12} \\ Z_{g22}\cdot Y_{21} & Z_{g22}\cdot Y_{22} \end{bmatrix} \tag{42}$$

where $Z_{g11}=Z_g(s)$, $Z_{g22}=Z_g(s_{p1})$.

$$\lambda_1=\frac{-b+\sqrt{b^2-4ac}}{2a};\quad \lambda_2=\frac{-b-\sqrt{b^2-4ac}}{2a} \tag{43}$$

where $a=1$; $b=-(Z_{g11}Y_{11}+Z_{g22}Y_{22})$; $c=Z_{g11}Z_{g22}(Y_{11}Y_{22}-Y_{12}Y_{21})$.

Fig. 10(a) and (b) show the Nyquist plots of grid-connected inverters systems when SCR changes. In Fig. 10(a), as SCR decreases from 3 to 1.2, both λ_1 and λ_2 do not surround $(-1, j0)$, which indicates the grid-connected inverter system adopting LADRC-PLL can keep stable. In Fig. 10(b), when SCR is 1.2, the Nyquist curve surrounds $(-1, j0)$, which indicates the grid-connected inverter system adopting PI-PLL is unstable. Table II shows the system stability under different SCRs.

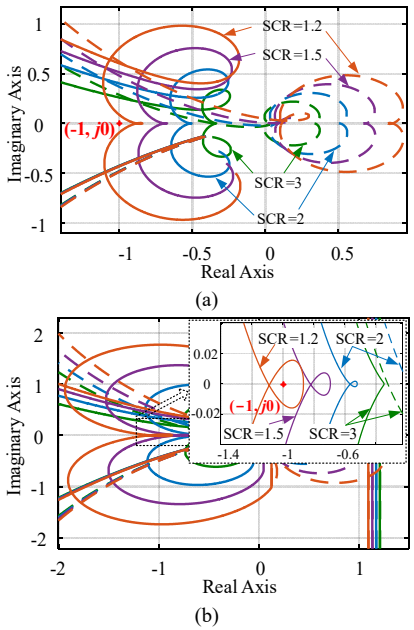

Fig. 10. The Nyquist plots when SCR is changed. (a) The grid-connected inverter with LADRC-PLL. (b) The grid-connected inverter with PI-PLL.

TABLE II
THE SYSTEM STABILITY UNDER DIFFERENT SCRS

SCR	The system adopting LADRC-PLL	The system adopting PI-PLL
3	Stable	Stable
2	Stable	Stable
1.5	Stable	Stable
1.2	Stable	Unstable

Therefore, compared with PI-PLL, the grid-connected inverter system adopting LADRC-PLL can keep stable under the weaker grid conditions.

The above conclusions can also be supported in the open-loop transfer function bode diagrams of LADRC-PLL and PI-PLL in Fig. 11. Compared with PI-PLL, the phase of the open-loop transfer function of LADRC-PLL near the cut-off frequency is significantly increased, making the phase margin increases 31°. Thus, compared with PI-PLL, the grid-connected inverter system adopting LADRC-PLL can keep stable in the weaker grid.

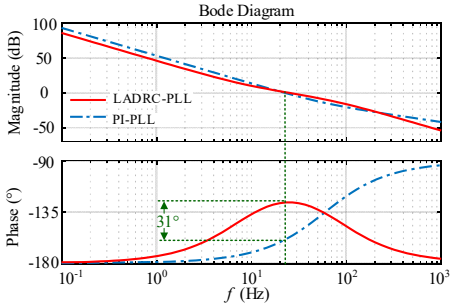

Fig. 11. The open-loop transfer function bode diagram.

This article has been accepted for publication in a future issue of this journal, but has not been fully edited. Content may change prior to final publication. Citation information: DOI 10.1109/TIE.2020.3044789, IEEE Transactions on Industrial Electronics

B. Robustness analysis of LADRC-PLL to control parameters

In order to study the robustness of LADRC-PLL to control parameters, the stability of the grid-connected inverter system adopting LADRC-PLL is discussed in Fig. 12 when b_0, ω_c and ω_0 are changed in the grid condition SCR = 1.2, respectively.

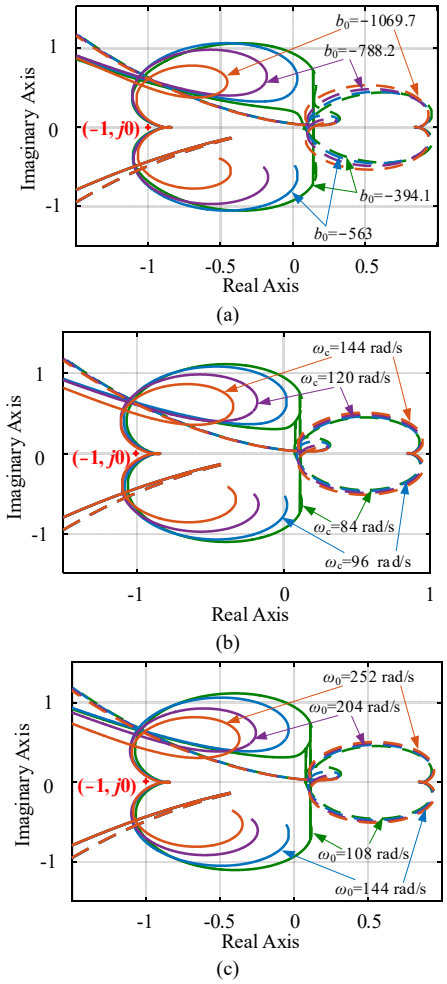

Fig. 12. The Nyquist plots when b_0, ω_c and ω_0 are changed. (a) b_0 is changed. (b) ω_c is changed. (c) ω_0 is changed.

Fig. 12(a) shows the Nyquist curves of the grid-connected inverter system adopting LADRC-PLL when b_0 is changed. As b_0 decreases from −394.1 to −1069.7, the Nyquist curves never surround $(-1, j0)$, which indicates the system remains stable.

The Nyquist curves are shown in Fig. 12(b) to reflect the influence of the changing ω_c on the system stability. With the ω_c increasing from 84 rad/s to 144 rad/s, the Nyquist curves are not surrounded $(-1, j0)$, which shows the system keeps stable.

The Nyquist curves when ω_0 is increased from 108 rad/s to 252 rad/s are shown in Fig. 12(c). The Nyquist curves do not surround $(-1, j0)$, which reflects the system remains stable.

In short, when b_0, ω_c and ω_0 are changed in a relatively wide range, respectively, the grid-connected inverter system adopting LADRC-PLL keeps stable. Thus, LADRC-PLL has good robustness to its control parameters.

C. Dynamic performance analysis

The dynamic performance of the system can be reflected by poles and zeros of the closed-loop transfer function. In this section, the dynamic performances according to the closed-loop transfer functions of LADRC-PLL and PI-PLL will be analyzed.

According to Fig. 4 and Fig. 5, the closed-loop transfer functions of the LADRC-PLL and PI-PLL are derived as below.

$$G_{\text{H\_LADRC}}(s) = \frac{V_m G_{\text{PLL}}(s)}{1 + V_m G_{\text{PLL}}(s)} \tag{44}$$

$$G_{\text{H\_PI}}(s) = \frac{V_m \left(k_{\text{p\_PLL}} s + k_{\text{i\_PLL}}\right)}{s^2 + V_m \left(k_{\text{p\_PLL}} s + k_{\text{i\_PLL}}\right)} \tag{45}$$

The dynamic performances of LADRC-PLL and PI-PLL can be analyzed through their poles and zeros of $G_{\text{H\_LADRC}}(s)$ and $G_{\text{H\_PI}}(s)$.

The poles and zeros diagram of $G_{\text{H\_LADRC}}(s)$ and $G_{\text{H\_PI}}(s)$ with the increasing of the amplitude of the grid voltage is shown in Fig. 13. The orange symbols present the poles and zeros of $G_{\text{H\_LADRC}}(s)$ and the blue symbols present the poles and zeros of $G_{\text{H\_PI}}(s)$ while the crosses present poles and the cycles present zeros. It can be noticed from Fig. 13 that the system dynamic performance of $G_{\text{H\_LADRC}}(s)$ is determined with three poles B, C, D, and E (There are zeros near poles A and F, therefore, poles A and F have no effect on the system dynamic performance due to pole-zero cancellation.). The system dynamic performance of $G_{\text{H\_PI}}(s)$ is determined with a pair of conjugate poles A' and B'.

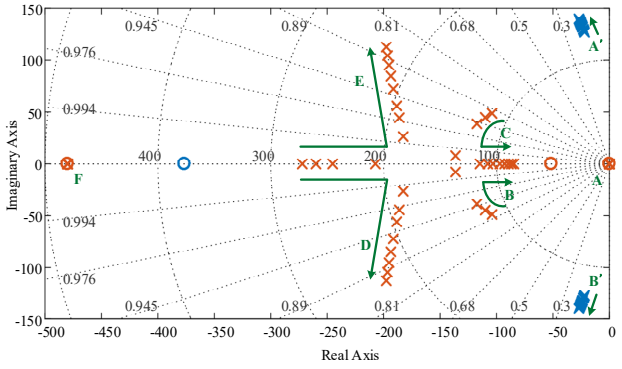

Fig. 13. The poles and zeros diagram of $G_{\text{H\_LADRC}}(s)$ and $G_{\text{H\_PI}}(s)$ with the increasing of the amplitude of the grid voltage.

The larger the damping ratio is, the less oscillatory the response is. It is shown in Fig. 13 that the damping ratios of the poles B, C, D, and E are larger than that of the poles A' and B'. Therefore, compared with PI-PLL, the response in LADRC-PLL is less oscillatory.

Moreover, the settling time is inversely proportional to the real part of the poles. The farther the poles are from the imaginary axis, the shorter the settling time is. Fig. 13 shows that the distances of the three poles B, C, D, and E to the imaginary axis are much larger than those of the poles A' and B'. Therefore, the settling time of LADRC-PLL is shorter than that of PI-PLL. It can be concluded that the dynamic performance of LADRC-PLL is better than that of PI-PLL.

In order to verify the above analysis, the simulation that the amplitude or phase of the grid voltage drops suddenly is carried out in the grid-connected inverter systems adopting PI-PLL and LADRC-PLL. The responses of the systems are shown in Fig. 14 and Fig. 15.

In Fig. 14, the amplitude of the grid voltage decreases 8% at 4 s. It can be noticed that the SCR has a great impact on the dynamic performance of both the grid-connected inverter systems adopting PI-PLL and LADRC-PLL. The weaker the grid becomes, the worse the dynamic performance of the system has. Compared with the grid-connected inverter system adopting PI-PLL, the settling time is shorter when the grid-connected inverter system adopts LADRC-PLL and the response in the grid-connected inverter system adopting LADRC-PLL is less oscillatory. Thus, the grid-connected inverter system adopting LADRC-PLL has better dynamic performance than that adopting

This article has been accepted for publication in a future issue of this journal, but has not been fully edited. Content may change prior to final publication. Citation information: DOI 10.1109/TIE.2020.3044789, IEEE Transactions on Industrial Electronics

PI-PLL when the amplitude of the grid voltage drops.

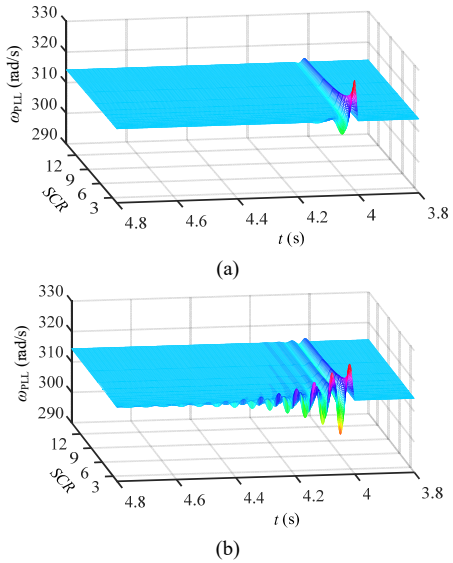

Fig. 14. The amplitude of the grid voltage decreases 8% at 4 s. (a) LADRC-PLL. (b) PI-PLL.

In Fig. 15, comparison results show that the settling time of the system adopting LADRC-PLL is shorter when the phase of the grid voltage suddenly changes 5° at 4 s; the response in the system adopting PI-PLL is more oscillatory. Thus, the system adopting LADRC-PLL has better dynamic performance when the phase of the grid voltage suddenly changes.

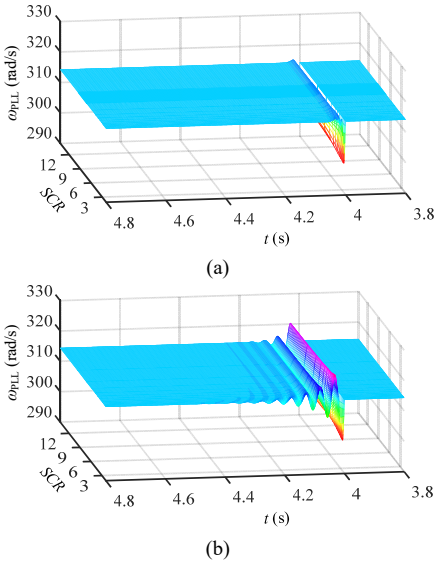

Fig. 15. The phase of the grid voltage suddenly changes 5° at 4 s. (a) LADRC-PLL. (b) PI-PLL.

It can be concluded that, compared with PI-PLL, the system adopting LADRC-PLL not only has better sub- and super-synchronous oscillation suppression ability, but also has better dynamic performance. The improvement of system stability is not achieved by sacrificing the system dynamic performance.

VI. Experimental Results

In order to further verify the correctness of the theoretical analysis, experiments have been carried out on the hardware-in-the-loop experimental platform, and the experimental parameters are consistent with the simulation parameters.

A. The system stability when SCR is changed

The experimental results of the grid-connected inverter system adopting PI-PLL when SCR is changed are shown in Fig. 16. When SCR is 3, the system is stable; when SCR is reduced to 1.2, the system occurs sub- and super-synchronous oscillation.

Fig. 17 shows the experimental results of the grid-connected inverter system adopting LADRC-PLL when SCR is changed. When SCR is 3 or 1.2, the system can keep stable.

Therefore, the experimental results verify that the grid-connected inverter with LADRC-PLL has better ability to suppress sub- and super-synchronous oscillation than PI-PLL.

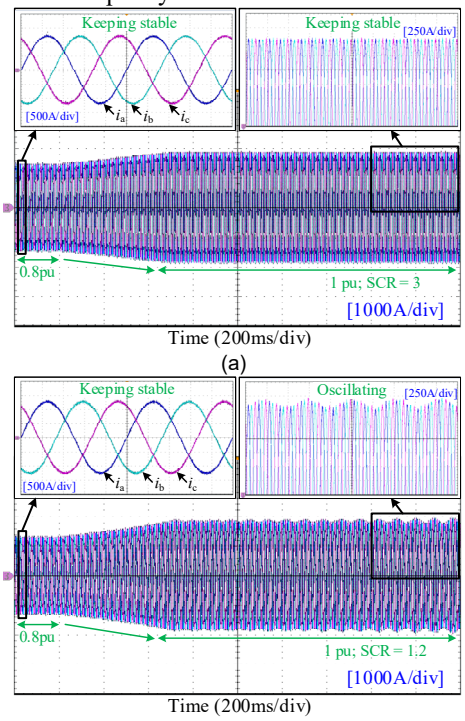

Fig. 16. The experimental results of the grid-connected inverter system adopting PI-PLL when SCR is changed. (a) SCR = 3. (b) SCR = 1.2.

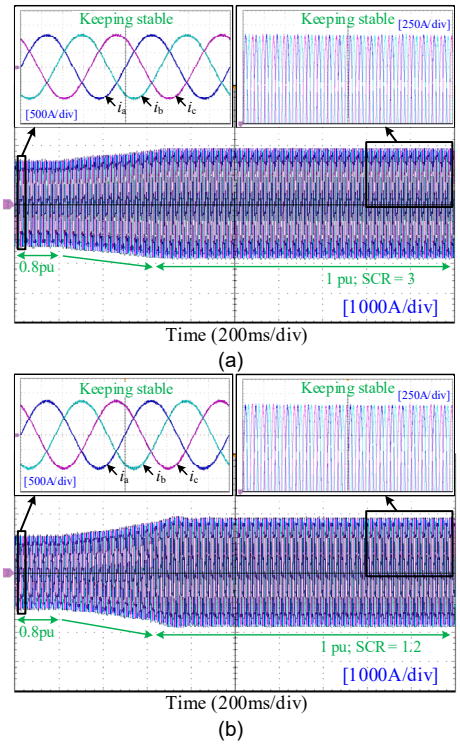

Fig. 17. The experimental results of the grid-connected inverter system adopting LADRC-PLL when SCR is changed. (a) SCR = 3. (b) SCR = 1.2.

This article has been accepted for publication in a future issue of this journal, but has not been fully edited. Content may change prior to final publication. Citation information: DOI 10.1109/TIE.2020.3044789, IEEE Transactions on Industrial Electronics

B. The robustness of LADRC-PLL to control parameters

Fig. 18 show the experimental results of the grid-connected inverter system adopting LADRC-PLL when b_0, ω_c and ω_0 are changed, respectively. As b_0 increases from −1069.7 to −394.1, ω_c increases from 84 rad/s to 144 rad/s, or ω_0 increases from 108 rad/s to 252 rad/s, the system keeps stable when SCR = 1.2.

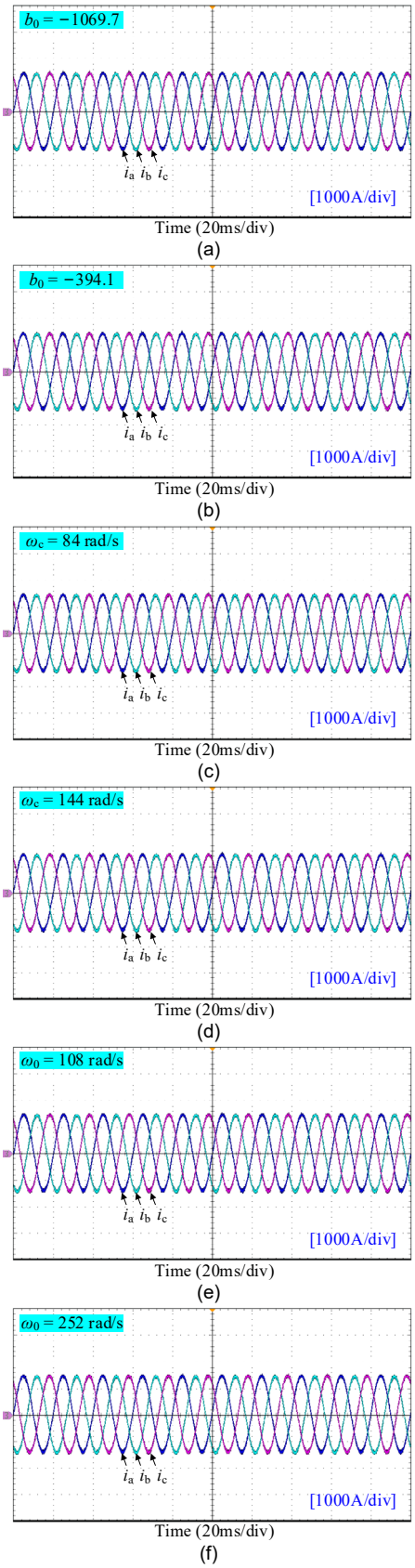

Fig. 18. The experimental results when control parameters of LADRC-PLL are changed. (a) b_0 = −1069.7. (b) b_0 = −394.1. (c) ω_c = 84 rad/s. (d) ω_c = 144 rad/s. (e) ω_0 = 108 rad/s. (f) ω_0 = 252 rad/s.

Therefore, the grid-connected inverter system adopting LADRC-PLL keeps stable when b_0, ω_c and ω_0 are changed in a relatively wide range, respectively. The experimental results verify that LADRC-PLL has good robustness to its control parameters.

C. The dynamic performance

To verify the system dynamic performance analyzed in Section V, the experiments that the grid voltage suddenly decreases are tested when SCR = 2. The experimental results of the grid-connected inverter systems adopting LADRC-PLL and PI-PLL are shown in Fig. 19 and Fig. 20.

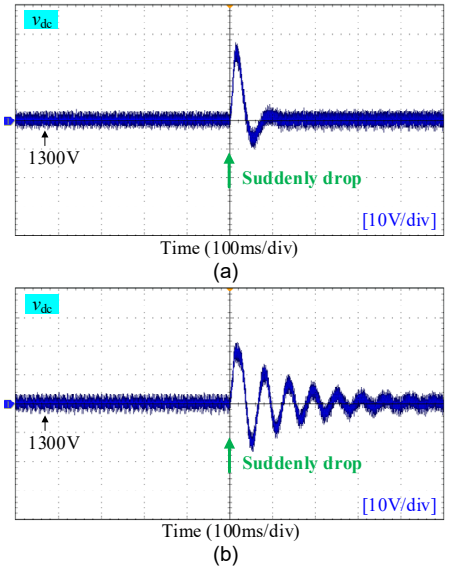

Fig. 19. The experimental results when the amplitude of the grid voltage suddenly drops. (a) LADRC-PLL. (b) PI-PLL.

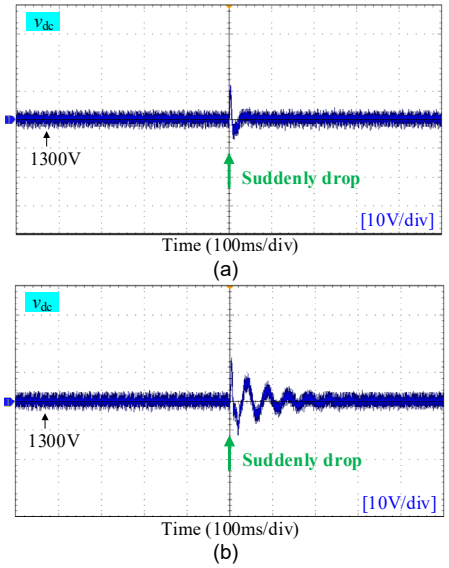

Fig. 20. The experimental results when the phase of the grid voltage suddenly decreases. (a) LADRC-PLL. (b) PI-PLL.

After the amplitude of the grid voltage suddenly decreases 8%, the comparison between Fig. 19(a) and (b) shows that the system adopting LADRC-PLL returns to stable operation faster with less oscillation than that adopting PI-PLL.

Similar to the results shown in Fig. 19, the system adopting LADRC-PLL returns to stable operation faster with less

oscillation than that adopting PI-PLL after the phase of the grid voltage suddenly changes 5 ° in Fig. 20.

Thus, the experimental results verify the theoretical analyses in Section V that, compared with PI-PLL, the grid-connected inverter system adopting LADRC-PLL has better dynamic performance.

VII. Conclusion

Considering the influence of LESO, voltage outer-loop, current inner-loop and frequency coupling, the admittance model of the grid-connected inverter with LADRC-PLL is derived by harmonic linearization method. The admittance characteristics, system stabilities and dynamic performances of grid-connected inverters with LADRC-PLL and PI-PLL are comparatively studied. The following conclusions are drawn:

1) After replacing PI-PLL with LADRC-PLL, the positive resistive components of the admittances are increased and the system damping is enhanced which reduces the risk of oscillation and improves the stability of the grid-connected inverter system in the sub- and super-synchronous frequency area.
2) The grid-connected inverter with LADRC-PLL has good robustness. When the input gain, control bandwidth or observer bandwidth of LADRC-PLL is changed in a relatively wide range, the system can still keep stable.
3) The grid-connected inverter with LADRC-PLL has better dynamic performance than that with PI-PLL. Compared with the grid-connected inverter system adopting PI-PLL, the settling time is shorter when the grid-connected inverter system adopts LADRC-PLL and the response in the grid-connected inverter system adopting LADRC-PLL is less oscillatory.
4) The above conclusions show that the grid-connected inverter with LADRC-PLL does not sacrifice the dynamic performance to improve system stability and has good robustness, which is very suitable for the system connected with the high proportion of renewable energy generator.

References

[1] J. Sun *et al.*, "Renewable energy transmission by HVDC across the continent: system challenges and opportunities," *CSEE Journal of Power and Energy Systems*, vol. 3, no. 4, pp. 353-364, Dec. 2017.

[2] K. Gu, F. Wu, and X. Zhang, "Sub-synchronous interactions in power systems with wind turbines: a review," *IET Renew. Power Gener.*, vol. 13, no. 1, pp. 4-15, Sep. 2019.

[3] Z. Xie, W. Wu, Y. Chen and W. Gong, "Admittance-based stability comparative analysis of grid-connected inverters with direct power control and closed-loop current control," *IEEE Transactions on Industrial Electronics*, Early Access Article.

[4] B. Wen, D. Boroyevich, R. Burgos, P. Mattavelli, and Z. Shen, "Analysis of D-Q Small-signal impedance of grid-tied inverters," *IEEE Trans. Power Electron.*, vol. 31, no. 1, pp. 675-687, Jan. 2016.

[5] M. Cespedes and J. Sun, "Impedance modeling and analysis of grid-connected voltage-source converters," *IEEE Trans. Power Electron.*, vol. 29, no. 3, pp. 1254–1261, Mar. 2014.

[6] W. Wu *et al.*, "Sequence-impedance-based stability comparison between VSGs and traditional grid-connected inverters," *IEEE Trans. Power Electron.*, vol. 34, no. 1, pp. 46-52, Jan. 2019.

[7] J. Sun and H. Liu, "Sequence impedance modeling of modular multilevel converters," *IEEE J. Emerg. Sel. Topics Power Electron.*, vol. 5, no. 4, pp. 1427-1443, Dec. 2017.

[8] W. Liu, Z. Lu, X. Wang, and X. Xie, "Frequency-coupled admittance modelling of grid-connected voltage source converters for the stability evaluation of subsynchronous interaction," *IET Renew. Power Gener.*, vol. 13, no. 2, pp. 285-295, Feb. 2019.

[9] Y. Li, L. Fan, and Z. Miao, "Wind in weak grids: low-frequency oscillations, subsynchronous oscillations, and torsional interactions," *IEEE Trans. Power Syst.*, vol. 35, no. 1, pp. 109-118, Jan. 2020.

[10] Y. Xu, Z. Gu, and K. Sun, "Characterization of subsynchronous oscillation with wind farms using describing function and generalized Nyquist criterion," *IEEE Trans. Power Syst.*, vol. 35, no. 4, pp. 2783-2793, Jul. 2020.

[11] Y. Xu, H. Nian, T. Wang, L. Chen, and T. Zheng, "Frequency coupling characteristic modeling and stability analysis of doubly fed induction generator," *IEEE Trans. Energy Convers.,* vol. 33, no. 3, pp. 1475-1486, Sep, 2018.

[12] H. Liu *et al.*, "Subsynchronous interaction between direct-drive PMSG based wind farms and weak AC networks," *IEEE Trans. Power Syst.*, vol. 32, no. 6, pp. 4708-4720, Nov. 2017.

[13] L. Fan, and Z. Miao, "Wind in weak grids: 4 Hz or 30 Hz oscillations?," *IEEE Trans. Power Syst.*, vol. 33, no. 5, pp. 5803-5804, Sep. 2018.

[14] Z. Xie *et al.*, "Modeling and control parameters design for grid-connected inverter system considering the effect of PLL and grid impedance," *IEEE Access*, vol. 8, pp. 40474-40484, Mar. 2020.

[15] X. Zhang, D. Xia, Z. Fu, G. Wang and D. Xu, "An improved feedforward control method considering PLL dynamics to improve weak grid stability of grid-connected inverters," *IEEE Trans. on Ind. Appl.*, vol. 54, no. 5, pp. 5143-5151, Sept.-Oct. 2018.

[16] Z. Xie, Y. Chen, W. Wu, W. Gong, and J. M. Guerrero, "Stability enhancing voltage feed-forward inverter control method to reduce the effects of phase-locked loop and grid impedance," *IEEE J. Emerg. Sel. Topics Power Electron.*, Early Access Article.

[17] M. S. El-Moursi, B. Bak-Jensen and M. H. Abdel-Rahman, "Novel STATCOM controller for mitigating SSR and damping power system oscillations in a series compensated wind park," *IEEE Trans. Power Electron.*, vol. 25, no. 2, pp. 429-441, Feb. 2010.

[18] M. Cespedes and J. Sun, "Adaptive control of grid-connected inverters based on online grid impedance measurements," *IEEE Trans. Sustain. Energ.*, vol. 5, no. 2, pp.516-523, Apr. 2014.

[19] D. Zhu, S. Zhou, X. Zou and Y. Kang, "Improved design of PLL controller for LCL-type grid-connected converter in weak grid," *IEEE Trans. Power Electron.*, vol. 35, no. 5, pp. 4715-4727, May 2020.

[20] S. Zhou et al., "An improved design of current controller for LCL-type grid-connected converter to reduce negative effect of PLL in weak grid," *IEEE J. Emerg. Sel. Topics Power Electron.*, vol. 6, no. 2, pp. 648-663, June 2018.

[21] K. Alawasa, Y. Mohamed, and W. Xu, "Active mitigation of subsynchronous interactions between PWM voltage-source converters and power networks," *IEEE Trans. Power Electron.*, vol. 29, no. 1, pp. 121-134, Jan. 2014.

[22] G. Li *et al.*, "Analysis and mitigation of subsynchronous resonance in series-compensated grid-connected system controlled by a virtual synchronous generator," *IEEE Trans. Power Electron.*, vol. 35, no. 10, pp. 11096-11107, Oct. 2020.

[23] J. Han, "From PID to active disturbance rejection control," *IEEE Trans. Ind. Electron.*, vol. 56, no. 3, pp. 900-906, Mar, 2009.

[24] Z. Gao, "Scaling and bandwidth-parameterization based controller tuning," in *Proceedings of the 2003 American Control Conference*, Denver, USA, Jun. 2003, pp. 1-8.

[25] B. Sun, and Z. Gao, "A DSP-based active disturbance rejection control design for a 1-kW H-bridge DC–DC power converter," *IEEE Trans. Ind. Electron.*, vol. 52, no. 5, pp. 1271-1277, Oct, 2005.

[26] Z. Song, Y. Tian, Z. Yan, and Z. Chen, "Direct power control for three-phase two-level voltage-source rectifiers based on extended-state observation," *IEEE Trans. Ind. Electron.*, vol. 63, no. 7, pp. 4593-4603, Jul, 2016.

[27] J. Lu, S. Golestan, M. Savaghebi, J. C. Vasquez, J. M. Guerrero, and A. Marzabal, "An enhanced state observer for DC-link voltage control of three-phase AC/DC converters," *IEEE Trans. Power Electron.*, vol. 33, no. 2, pp. 936-942, Feb. 2018.

[28] B. Du, T. Zhao, S. Han, L. Song, and S. Cui, "Sensorless control strategy for IPMSM to reduce audible noise by variable frequency current injection," *IEEE Trans. Ind. Electron.*, vol. 67, no. 2, pp. 1149-1159, Feb. 2020.

[29] Y. Cao, Q. Zhao, Y. Ye and Y. Xiong, "ADRC-based current control for grid-tied inverters: design, analysis, and verification," *IEEE Trans. on Ind. Electron.*, vol. 67, no. 10, pp. 8428-8437, Oct. 2020.

[30] S. Gude, and C. Chu, "Dynamic performance improvement of multiple delayed signal cancelation filters based three-phase enhanced-PLL," *IEEE Trans. Ind. Appl.*, vol. 54, no. 5, pp. 5293-5305, Sep 2018.

[31] M. Ramezani, S. Golestan, S. Li, and J. M. Guerrero, "A simple approach to enhance the performance of complex-coefficient filter-based PLL in grid-connected applications," *IEEE Trans. Ind. Electron.*, vol. 65, no. 6, pp. 5081-5085, Jun. 2018.

[32] P. Chittora, A. Singh, M. Singh, "Adaptive EPLL for improving power quality in three-phase three-wire grid-connected photovoltaic system," *IET Renew. Power Gener.*, vol. 13, no. 9, pp. 1595-1602, Apr. 2019.

Zhiwei Xie was born in Hunan, China, 1994. She received the B.S. degree in electronic information engineering from Changsha University of Science and Technology, Changsha, China, in 2016. Currently, she has been working toward the Ph.D. degree in electrical engineering from Hunan University, Changsha, China.

Her research interests include power electronics converter, distributed generation.

Yandong Chen (S'13-M'14-SM'18) was born in Hunan, China, in 1979. He received the B.S. and M.S. degree in instrument science and technology from Hunan University, Changsha, China, in 2003 and 2006, respectively, and the Ph.D. degree in electrical engineering from Hunan University, Changsha, China, in 2014. He is currently a Professor in the College of Electrical and Information Engineering, Hunan University, Changsha.

His research interests include power electronics for microgrid, distributed generation, power supply, and energy storage. Dr. Chen is a recipient of the 2014 National Technological Invention Awards of China, and the 2014 WIPO-SIPO Award for Chinese Outstanding Patented Invention. He is a Senior Member of IEEE PES & PELS.

Wenhua Wu (S'16-M'20) was born in Hunan, China, in 1991. He received the B.S. and Ph.D. degrees in electrical engineering from Hunan University, Changsha, China, in 2014 and 2019, respectively. He is currently a Postdoctoral Researcher in electrical engineering with Hunan University.

His research interests include power electronics, modeling, and control of renewable power generation systems.

Wenlan Gong was born in Guangxi, China, 1992. She received the M.S. degree from the College of Electrical and Information Engineering, Hunan University, Changsha, China, in 2019. Currently, she has been working in Electric Power Research Institute of Guangxi Power Grid Co. Ltd., Nanning, China.

Her research context includes power electronics converter, reactive power compensation, distributed generation.

Leming Zhou (M'17) was born in Hunan, China, in 1989. He received the B.S. and Ph.D. degrees in electrical engineering from Hunan University, Changsha, China, in 2011 and 2016, respectively. Currently, he has been working an Associate Professor in electrical engineering from Hunan University, Changsha, China.

His research interests include power electronics, electric power green transformation, distributed generation, and marine special power supply.

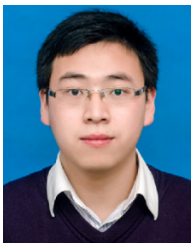

Xiaoping Zhou (S'16-M'19) was born in Jiangxi, China, 1990. He received the B.S. and Ph. D. degrees in electrical engineering from Hunan University, Changsha, China, in 2013 and 2018, respectively. He is currently working as an Associate Professor of electrical engineering with Hunan University, Changsha, China.

His research interests include HVDC systems, distributed generation, microgrid, power quality, and energy storage.

Josep M. Guerrero (S'01-M'04-SM'08-FM'15) received the B.S. degree in telecommunications engineering, the M.S. degree in electronics engineering, and the Ph.D. degree in power electronics from the Technical University of Catalonia, Barcelona, in 1997, 2000 and 2003, respectively. Since 2011, he has been a Full Professor with the Department of Energy Technology, Aalborg University, Denmark.

His research interests mainly include power electronics, distributed energy-storage, and microgrids. Prof. Guerrero is an Associate Editor for the IEEE TRANSACTIONS ON POWER ELECTRONICS, the IEEE TRANSACTIONS ON INDUSTRIAL ELECTRONICS, and the IEEE Industrial Electronics Magazine, and an Editor for the IEEE TRANSACTIONS on SMART GRID and IEEE TRANSACTIONS on ENERGY CONVERSION. In 2014, 2015, and 2016 he was awarded by Thomson Reuters as Highly Cited Researcher, and in 2015 he was elevated as IEEE Fellow for his contributions on distributed power systems and microgrids.